DOI: 10.37190/abb/231629

Effects of the Thorax and Passive Lumbar Paraspinal Muscles on the Stability of the Kyphotic Spine Based on U-Net

Jiameng Gong[1], Rongchang Fu[1,*], Jintao Li[1], Kaitao Li[1]

[1]School of Mechanical Engineering, Xinjiang University, Urumqi 830017, Xinjiang, China

[*]Corresponding author: Rongchang Fu, School of Mechanical Engineering, Xinjiang University, Urumqi 830017, Xinjiang, China, e-mail address: 2781642414@qq.com

Submitted: 18th June 2026

Accepted: 24th August 2026

Abstract:

Purpose: To investigate the passive biomechanical effects of the thoracic cage and passive lumbar paraspinal muscles on the stability of the kyphotic spine. Methods: Patient-specific clinical CT data and a U-Net convolutional neural network were utilized to segment the lumbar paraspinal muscles. Two finite element (FE) models were developed: a composite model including the intact thoracic cage and passive muscles (S1), and a spine-only model (S2). Axial rotation, lateral bending, and flexion-extension conditions were simulated to compare the overall spinal displacement and rotation angles of each vertebra relative to the pelvis between the two models. Results: The restriction of spinal displacement by the thoracic cage and passive muscles demonstrated significant direction specificity: the strongest constraint occurred in axial rotation (19.6%), followed by lateral bending (8.1%) and flexion-extension (1.3%). Segmentally, changes in rotation angles exhibited regional heterogeneity. Under the axial rotation condition, upper thoracic (T1-T5) rotation angles decreased significantly (>20%), while rotation angles from the thoracolumbar junction downwards (T10-L5) increased (1.27%–8.33%). Under lateral bending and flexion-extension conditions, rotation angles showed a decreasing trend across all segments (decreasing by 3.77%–14.29% and 1.39%–7.00%, respectively). Conclusions: The thoracic cage and passive paraspinal muscles significantly restrict axial rotation; however, maintaining sagittal balance relies primarily on active musculature. This anti-rotation mechanism may induce a "local anchoring and distal compensation" effect, which may increase lower lumbar mobility. In clinical practice, conservative treatment should adopt a dual strategy of anti-rotation bracing combined with active anti-flexion muscle strengthening, while maintaining high vigilance for the risk of secondary degeneration in the lower lumbar spine.

Keywords:

Thoracic cage; Paraspinal muscles; Kyphosis; Deep learning; Finite element analysis

1. Introduction

Spinal kyphosis is a spinal deformity characterized primarily by an abnormally increased sagittal curvature, which can result from various etiologies including degenerative changes, vertebral fractures, muscle dysfunction, or ankylosing spondylitis [15],[38]. Severe kyphotic deformity not only disrupts sagittal balance but also significantly impairs patients' physical function and quality of life. In spinal biomechanics research, finite element analysis has become one of the most effective tools for simulating spinal pathologies and evaluating mechanical responses due to its controllability and reproducibility[7],[32]. However, traditional static and dynamic finite element analyses of the spine, often aiming to reduce computational costs or focus on local segments, habitually simplify the model into an isolated spinal structure, neglecting the influence of the thoracic cage and lumbar paraspinal muscles. This simplification compromises the reliability of simulation results to some extent.

As an indispensable supporting structure for the thoracolumbar spine, the thoracic cage is composed of the sternum, ribs, and costovertebral joints. It not only plays a role in respiratory movements and organ protection but also holds a central position in sharing spinal loads and maintaining three-dimensional stability[1],[17],[24]. The mathematical model by Andriacchi et al.[2]was the first to theoretically demonstrate that the thoracic cage significantly enhances the overall stiffness of the spine. Subsequently, an *in vitro* experimental study by Brasiliense et al.[5] further quantified that an intact thoracic cage provides approximately 78% of the mechanical stability for the thoracolumbar region. Research by Oda et al. [23]also indicated that removal of the thoracic cage leads to a substantial increase in thoracolumbar range of motion (ROM). In recent years, a finite element analysis by Jia et al. [12]confirmed that the thoracic cage plays a more significant role in maintaining stability in patients with scoliosis compared to healthy individuals. However, the normal spine exhibits relatively symmetrical rib-cage morphology and load transfer. Scoliosis is a three-dimensional deformity characterized primarily by coupled coronal curvature and vertebral axial rotation, often accompanied by rib-cage asymmetry. In contrast, kyphosis is characterized mainly by increased sagittal curvature and may involve vertebral wedging, altered rib inclination, and changes in costovertebral relationships. These morphological differences may alter rib–vertebra coupling and load sharing between the thoracic cage and spine. Therefore, findings from normal or scoliotic spines cannot be directly extrapolated to kyphotic deformity, and the specific contribution of the thoracic cage to the stability of kyphotic spines remains insufficiently investigated.

As the core component of the spinal dynamic stabilization system, the lumbar paravertebral muscles also play an indispensable role[25]. Previous studies have often focused on the active contractile forces of muscles while underestimating the critical supportive efficacy of passive muscle tension under specific mechanical environments. The finite element study by Arjmand et al. [3]pointed out that with increasing trunk flexion angle, the passive muscle-ligament complex can bear up to 77% of the external bending moment, highlighting the decisive role of passive tissues in load sharing. However, in traditional spinal finite element models, the lumbar paravertebral muscles are frequently simplified as one-dimensional spring elements connecting anatomical origin and insertion points. This "point-to-point" simplification neglects the true spatial curvature and contact constraints of the muscles: the study by Stokes et al. [30]demonstrated that the line of action of muscle forces changes dynamically with spinal morphology; Kang et al.[14]also confirmed that the physiological volume of muscles is a key geometric variable regulating load distribution. One-dimensional line elements cannot simulate the "wrapping effect" of solid muscles around the vertebrae or the lateral supporting forces generated by volumetric deformation. Therefore, employing three-dimensional solid elements to construct muscle models is a superior choice for enhancing simulation accuracy.

Although three-dimensional solid muscle modeling offers clear advantages, its geometric reconstruction presents challenges. Traditional methods often rely on anatomical atlases to manually outline muscle contours using three-dimensional software[16]. However, for patients with kyphosis accompanied by severe skeletal deformities and asymmetric degeneration of the lumbar paravertebral muscles, this generalized modeling approach introduces significant morphological errors. Obtaining patient-specific, realistic muscle morphology requires direct segmentation from individual medical images. Given that manual segmentation of a large number of continuous images is time-consuming and highly subjective, Wesselink et al. [34]confirmed that using convolutional neural networks (such as U-Net) for automatic segmentation of lumbar paravertebral muscles can substantially reduce time costs while ensuring accuracy. However, facing the blurred anatomical boundaries of muscles caused by spinal deformities, whether this network can maintain high-precision segmentation under complex pathological morphologies and support high-fidelity three-dimensional solid modeling requires further investigation.

In summary, this study employs the U-Net convolutional neural network to automatically segment the lumbar paravertebral muscles from patient CT data. Specifically, the core muscles directly related to lumbar stability are selected, including the erector spinae (ES) and multifidus (MF) located posterior to the spine, and the psoas major (PM) located laterally to the vertebral bodies. Based on this, a composite finite element model incorporating the thoracic cage and passive lumbar paravertebral muscles (S1), along with a control model representing the spinal structure alone (S2), was constructed using reverse engineering techniques. The aim is to quantitatively investigate the influence of the thoracic cage and passive lumbar paravertebral muscles on the stability of the kyphotic spine under different loading conditions. The findings are expected to deepen the understanding of the differential contributions of the thoracic cage and passive lumbar muscles in maintaining spinal stability under various movement directions and to provide theoretical references for clinical intervention and rehabilitation strategies for spinal kyphosis.

2. Materials and Methods

2.1 Dataset Preparation

The raw data for this study originated from CT scan images of a 22-year-old male patient with idiopathic spinal kyphosis (height 172 cm, weight 70 kg, kyphosis Cobb angle 48°, proximal thoracic Cobb angle 27°, thoracolumbar Cobb angle 42°, lumbar Cobb angle 34°, the apex of the deformity was at T8, with no evidence of vertebral wedging or vertebral fracture, no obvious scoliosis in the coronal plane) admitted to the Sixth Affiliated Hospital of Xinjiang Medical University.The dataset comprised 720 axial cross-sectional images in DICOM format, from which 180 slices containing the lumbar spine were selected. Due to significant overlap and adhesion in grayscale values among muscles, fat, and surrounding tissues, this study introduced the publicly available Project Pillar muscle segmentation guidelines [26]as the labeling reference, which provide standardized segmentation boundaries for the multifidus, erector spinae, and psoas major muscles in both healthy individuals and patients with low back pain. Based on these guidelines, labeling was performed using ITK-SNAP software, as shown in Figure 1. This strategy leverages standardized anatomical constraints to effectively reduce subjectivity in annotation, thereby providing high-quality label data for the subsequent U-Net convolutional neural network.

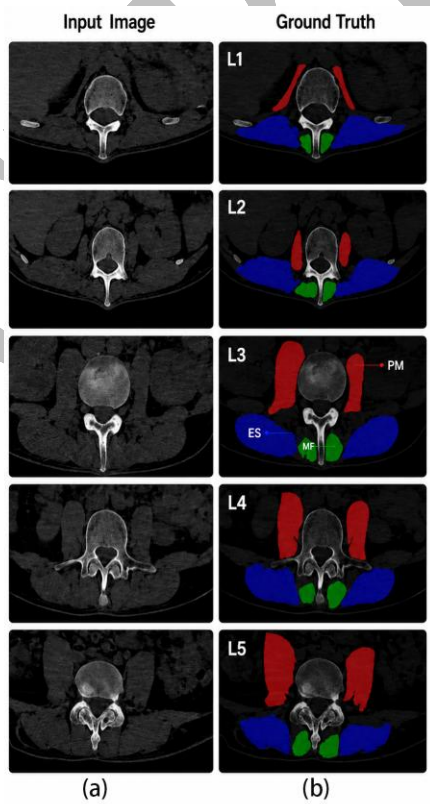

Figure 1: Annotation of lumbar paravertebral muscles incorporating the Project Pillar muscle segmentation guidelines. (a) Input image; (b) Ground truth, where red represents PM, blue represents ES, and green represents MF.

2.2 Image Preprocessing and Dataset Partitioning

The input image dataset used in this study was in DICOM format, with a slice thickness of 1 mm, an in-plane pixel spacing of 0.9766 × 0.9766 mm, and an image matrix of 512 × 512. To meet the input requirements of the PyTorch deep learning framework, Python scripts were used to parse the input images and corresponding ground truth labels from the three-dimensional format into two-dimensional grayscale PNG format images. To ensure the objectivity and reliability of model evaluation, this study adopted a cross-validation approach for dataset partitioning. Three researchers independently set random seeds to randomly allocate the 180 sample sets into training (132 sets), validation (28 sets), and test (20 sets) sets, resulting in three random partitioning schemes. The final model evaluation results were obtained by averaging the evaluation outcomes across these three random experiments.

2.3 U-Net Network Architecture

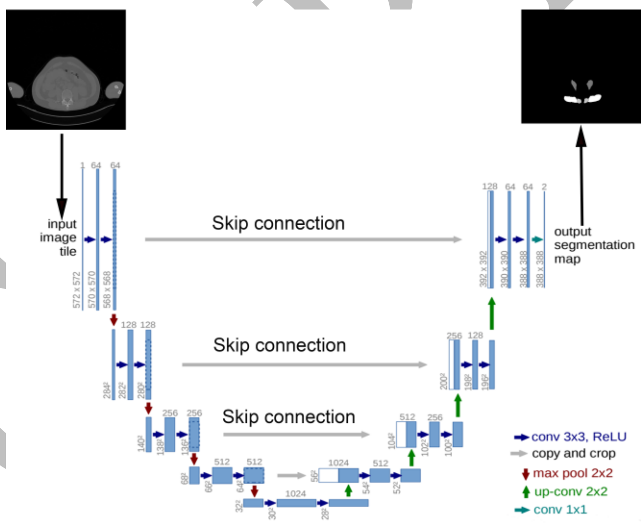

Figure 2: Schematic diagram of the U-Net network architecture[28].

In this study, U-Net was selected as the core segmentation model. As a benchmark architecture in the field of medical image segmentation, U-Net's classic encoder-decoder design and its iconic "skip connection" mechanism effectively integrate deep semantic features with shallow high-resolution spatial information[28]. In lumbar CT images, the lumbar paravertebral muscles often exhibit severe adhesion to surrounding adipose tissue, with poorly defined boundaries. U-Net's feature fusion strategy maximizes the recovery of spatial information lost during downsampling, enabling superior localization accuracy in such soft tissue segmentation tasks with blurred boundaries[4]. This high-precision extraction of anatomical boundaries lays a solid geometric foundation for the subsequent construction of reliable spinal biomechanical models.

2.4 Model Training and Evaluation Metrics

In this study, the construction and training of the network model were carried out using the PyTorch deep learning framework and completed on a computing environment equipped with CUDA hardware acceleration (NVIDIA RTX 4060 GPU). The model input was a single-channel grayscale image, and the number of output channels was set to 4 (covering background and the three target muscles). During the training phase, the batch size was set to 4, the initial learning rate was set to 0.001, and the model was trained for a total of 100 epochs. To accelerate model convergence and optimize parameter updates, the Adam optimizer was selected**Błąd! Nieznany argument przełącznika.**. This study employed a transfer learning strategy, initializing the U-Net encoder with pre-trained weights from the ImageNet large-scale dataset to enhance the model’s feature extraction capability for complex anatomical structures in medical imaging. Furthermore, given the significant class imbalance between background and target muscle pixels in medical images, a hybrid loss function combining cross-entropy loss and Dice loss was constructed. This strategy not only ensured stable model convergence at the pixel level but also enhanced the precision of local boundary segmentation for soft tissues[10].

To objectively quantify the segmentation performance of the deep learning model, this study adopted the Dice similarity coefficient, the core evaluation metric in medical image semantic segmentation tasks. This metric primarily measures the spatial overlap between the model’s prediction set (A) and the manually annotated ground truth set (B)[20], and its calculation formula is as follows:

$$Dice(A,B) = \frac{2|A \cap B|}{|A+B|} \tag{1}$$

where |A| and |B| represent the size of the pixel set in the predicted mask and the ground truth label, respectively. The Dice coefficient ranges from 0 to 1; a value closer to 1 indicates a higher degree of agreement between the algorithm's prediction and the actual anatomical structure.

2.5 Experimental Results and Analysis

2.5.1 Model Convergence

Figure 3 illustrates the convergence curves across three random experiments. The results indicate that both training and validation losses exhibit a synchronized downward trend, while the accuracy steadily increases amidst initial fluctuations and eventually converges at a high level.

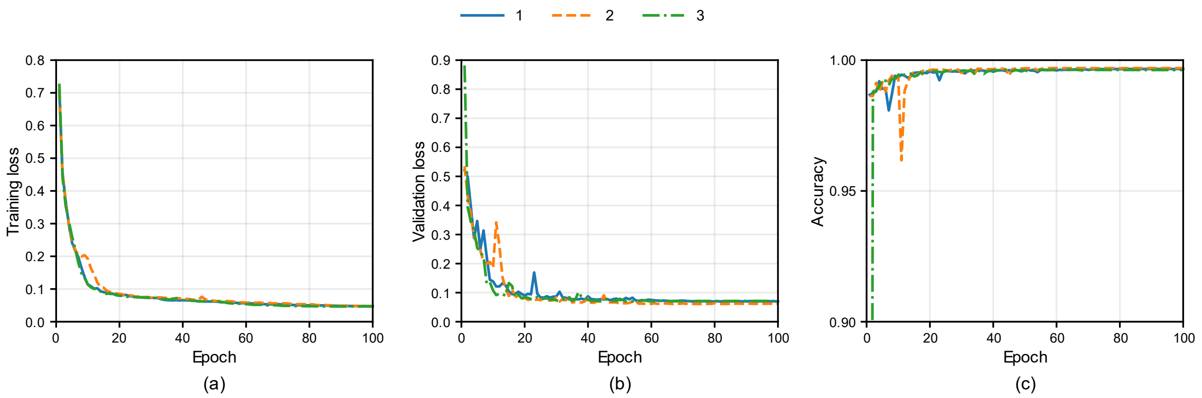

Figure 3: Loss and accuracy convergence curves of model training. Comparison of (a) training loss, (b) validation loss, and (c) accuracy across three random experiments (Trial 1, 2, and 3).

2.5.2 2D U-Net Prediction and Analysis of the "Spectral Bias" Effect

Figure 4 presents a comparison between the ground truth labels (Figure b) and the predictions from the U-Net model (Figure c) for representative samples from the test set. It can be observed that the model predictions exhibit a high degree of agreement with the ground truth , indicating satisfactory training performance. However, it can also be noted that during manual annotation, constrained by the limited resolution of medical images and the cubic geometry of voxels (partial volume effect), delineation in the sagittal or coronal plane often results in noticeable "jagged" or layered discontinuous artifacts at the edges in the two-dimensional axial images[6]. Nonetheless, the predictions from the U-Net model demonstrate smoother and more continuous boundary morphology.

This phenomenon can be well explained by the "spectral bias" property of deep neural networks. As indicated by the study of Rahaman et al.[27], when fitting data, neural networks tend to prioritize learning low-frequency global continuous components while exhibiting a strong inertia against high-frequency components representing noise or discretization artifacts. Consequently, during the training process in this study, U-Net effectively acted as a nonlinear low-pass filter, accurately recovering the macroscopic topology of the muscles while automatically smoothing the discrete stepped artifacts introduced by voxelization in the manual labels.

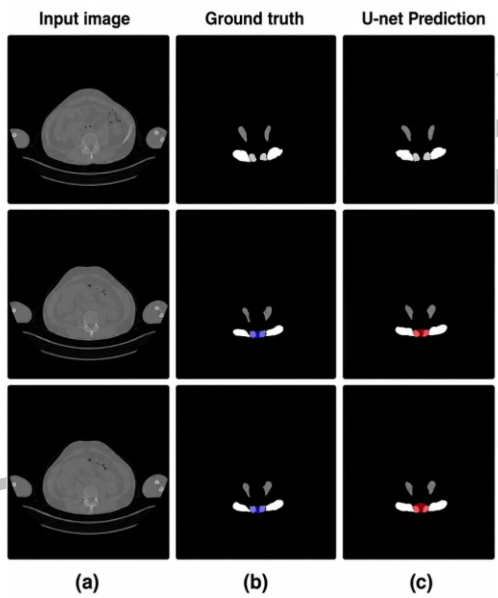

Figure 4. Comparison of segmentation results on test set samples. (a) Input image; (b) Ground truth ; (c) U-Net predicted labels. The blue regions indicate jagged boundaries present in the ground truth labels, while the red regions indicate the relatively smooth boundaries predicted by the U-Net network.

2.5.3 Test Evaluation

The U-Net network demonstrated good segmentation performance for the lumbar paraspinal muscles on the test-slice set of the present case, with a mean Dice coefficient of 0.88175 across three different random-split experiments (Figure 5). These results indicate that, under the conditions of the present case and slice-level data partitioning, U-Net can consistently extract the primary morphological features of the paraspinal muscles and provide a basis for reconstructing their three-dimensional geometry in the subsequent finite element model.

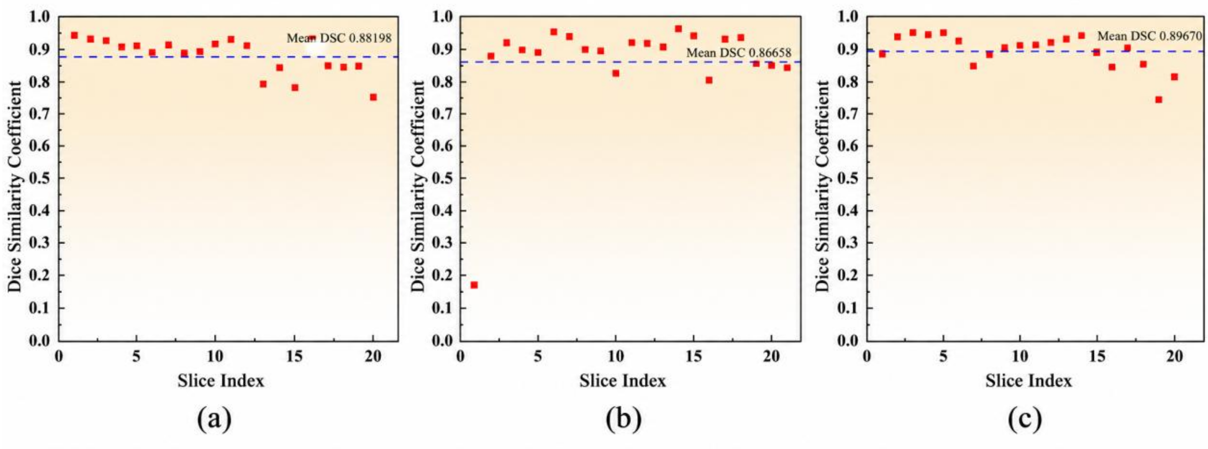

Figure 5. Dice results on the test set. (a) First experiment; (b) Second experiment; (c) Third experiment.

2.6 3D Reconstruction and Preprocessing of the Finite Element Geometric Model

Based on the aforementioned training performance and analysis of local edge discrepancies, this study further extended the evaluation dimension to three-dimensional space to investigate the morphological differences between the predictions of the U-Net convolutional neural network and the ground truth labels in three dimensions. To this end, the sample group that achieved the optimal Dice coefficient in the test evaluation was selected as the representative, and batch prediction was performed on all its input image sequences. To ensure the accuracy of the physical scale during three-dimensional reconstruction, the two-dimensional PNG masks output by the algorithm were reassigned the spatial coordinates and voxel spacing parameters of the original data and converted to NIfTI format. As shown in Figure 6, the ground-truth annotations (Figure 6a) exhibit local surface discontinuities in the reconstructed geometry due to slice-by-slice annotation and the voxelization stair-step effect, whereas the U-Net predictions (Figure 6b) demonstrate superior surface continuity. Compared with conventional manual or atlas-based muscle reconstruction, this deep-learning-based segmentation method directly extracts paraspinal muscle boundaries from the patient's own images, preserving individualized spatial relationships of muscle contours, volume, and their alignment with the vertebrae, while reducing observer variability and template morphological bias. The resulting continuous, smooth, and patient-specific muscle geometry provides a reliable geometric foundation for subsequent Boolean operations, volume meshing, material property assignment, and finite element analysis.

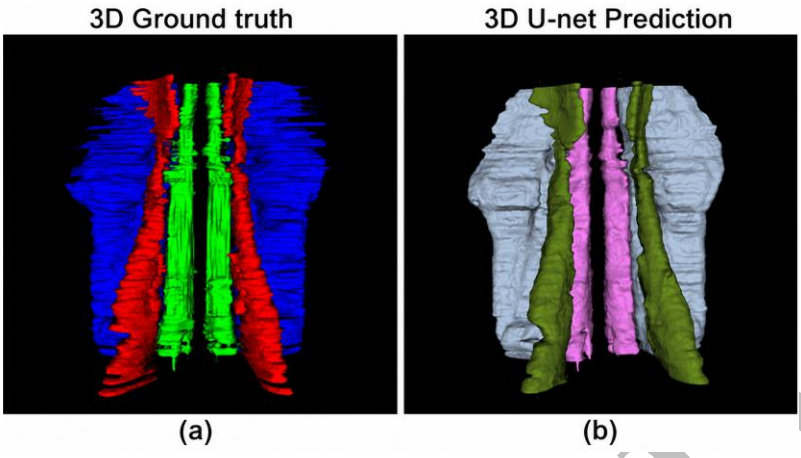

Figure 6: Three-dimensional reconstruction of lumbar paravertebral muscles. (a) Ground truth; (b) U-Net predictions.

2.7 Construction of the Spine-Thorax-Pelvis Three-Dimensional Geometric Model

First, the patient's continuous CT sequences in DICOM format were imported into Mimics 21.0 (Materialise, Belgium). Using threshold segmentation, the three-dimensional surface models of the sternum, ribs, T1–L5 vertebrae, pelvis, and partial femur were initially extracted and reconstructed. Subsequently, these skeletal models, along with the lumbar paraspinal muscle models automatically segmented by the aforementioned U-Net convolutional neural network, were imported into Geomagic Freeform 2019 (3D Systems, USA). At this stage, the model surfaces were smoothed, costal cartilages were constructed, and the sacrum, ilium, and femur were separated to restore authentic osteoarticular boundaries. To meet the high-quality geometric requirements for subsequent finite element analysis, the pre-processed models were exported in STL format to Geomagic Studio 12.0 (Geomagic, USA) for NURBS surface fitting and topological optimization. Following this, the models were exported as IGS solids into SolidWorks 2022 (Dassault Systèmes, France), where CAD modeling functions were utilized to further construct the intervertebral discs and facet joint cartilages. According to the anatomical basis in reference[Błąd! Nieznany argument przełącznika.], the volume ratio of the annulus fibrosus matrix to the nucleus pulposus in the intervertebral disc was set to 60% and 40%, respectively. Finally, the fully assembled geometric model was imported into HyperMesh 14.0 (Altair, USA) for complex mesh generation and material property preprocessing. During this phase, key ligamentous structures, including the anterior longitudinal ligament (ALL), posterior longitudinal ligament (PLL), ligamentum flavum (LF), capsular ligament (CL), intertransverse ligament (ITL), interspinous ligament (ISL), and supraspinous ligament (SSL), were sequentially constructed[8]. Based on these steps, a composite finite element model incorporating the complete thoracic cage and passive lumbar paraspinal muscles (S1) and a standalone spinal model (S2) were established, as shown in Figure 7.

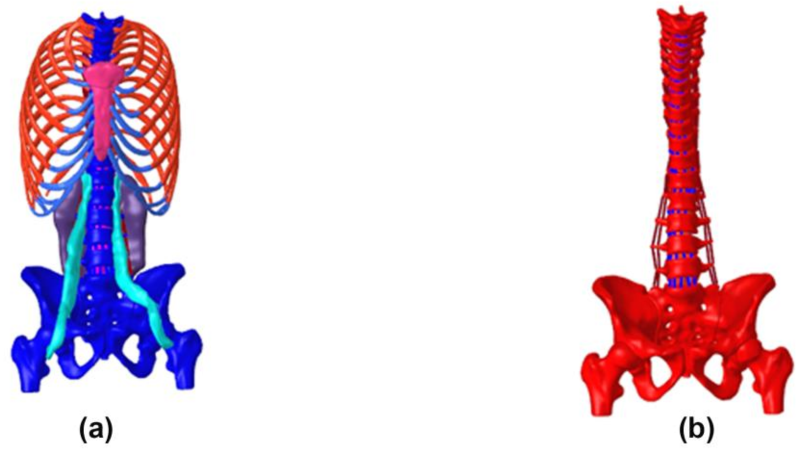

Figure 7: Diagrams of S1 and S2 models. (a) S1 model; (b) S2 model.

2.8 Element Type Definition and Material Property Assignment

During the finite element mesh generation phase, to balance computational accuracy and efficiency, this study adopted differentiated element types for different anatomical structures. The cortical bone of the vertebral bodies was modeled using three-node triangular linear shell elements with a thickness of 1 mm[31], a strategy that effectively prevents severe mesh distortion at complex geometric interfaces. The trabecular bone was filled using four-node tetrahedral solid elements. The sternum and ribs employed the same element strategy as the vertebral bodies, with their cortical bone thickness also set to 1 mm[31].The nucleus pulposus, annulus fibrosus were finely meshed using ten-node quadratic tetrahedron. The articular cartilage, costal cartilage, and muscles were modeled using eight-node hexahedral solid elements.

Regarding material constitutive relationships and model interactions, all ligaments were defined as linearly elastic and isotropic materials. To simulate realistic biomechanical load transfer, shared node connections were used at the attachment sites between muscles and lumbar vertebral bodies[16]. Meanwhile, tie constraints preventing relative slippage were established at the adjacent joint regions between ribs and vertebral bodies, ribs and costal cartilage, and costal cartilage and sternum[12]. The element types and linear elastic material properties employed in this model are presented in Table 1[12],[14],[22],[36].

Table 1. Element types and material properties of the model components

Components	Element type	Elastic modulus (MPa)	Poisson's ratio	Cross-sectional area (mm^2)
Vertebral cortical bone	S3	12000	0.3	
Vertebral trabecular bone	C3D4	100	0.2	
Endplate	S4R	24	0.4	
Annulus fibrosus matrix	C3D10	4.2	0.3	
Nucleus pulposus	C3D10	1	0.49	
Articular cartilage	C3D8R	20	0.3	
ALL	T3D2	7.8	0.3	63.7
PLL	T3D2	10	0.3	20
LF	T3D2	15	0.3	40
ISL	T3D2	10	0.3	40
SSL	T3D2	8	0.3	30
ITL	T3D2	10	0.3	1.8
CL	T3D2	20	0.3	30
Rib cortical bone	S3	12000	0.3	
Rib trabecular bone	C3D4	150	0.3	
Costal cartilage	C3D8R	300	0.4	
Sternal cortical bone	S3	12000	0.3	
Sternal trabecular bone	C3D4	150	0.3	
Muscles	C3D8R	0.045	0.449	

2.9 Model Validation

2.9.1 Mesh Sensitivity Verification

To validate the S1 and S2 models, a mesh sensitivity analysis was first performed to eliminate the influence of mesh size on the computational accuracy of the finite element analysis. The global base mesh sizes were set to three gradients: 0.8 mm, 1.0 mm, and 1.2 mm. Regarding the boundary conditions, all degrees of freedom of the pelvis were fully fixed, and a vertical axial compressive load of 40 N was applied to the superior endplate surface of the L1 vertebral body as a test load (this load served as a nominal numerical test load rather than a physiological loading condition). Subsequently, the peak von Mises stresses of the lumbar cortical bone, trabecular bone, nucleus pulposus, and annulus fibrosus matrix within the L1–L5 segments were extracted and compared across the different mesh sizes. Meanwhile, the maximum displacement of the model and the rotation angles of the T1 and L1 vertebrae relative to the pelvis were further compared, and mesh independence was comprehensively evaluated from both stress and kinematic perspectives.

According to the finite element verification criteria, if the relative difference in stress results between adjacent mesh gradients is less than 5%, the model is considered to have achieved mesh convergence and is thus validated[13].

Table 2. Peak von Mises stress (MPa), maximum displacement, and specific segmental rotation angles (°) at different mesh sizes (mm).

Model	Parameter	0.8	1.0	1.2	Relative difference (0.8 vs. 1.0)	Relative difference (1.0 vs. 1.2)
S1	Vertebral cortical bone (MPa)	10.768	11.136	11.487	3.42%	3.15%
	Vertebral trabecular bone(MPa)	8.516	8.743	8.963	2.67%	2.52%
	Nucleus pulposus(MPa)	0.345	0.356	0.368	3.19%	3.37%
	Annulus fibrosus matrix(MPa)	0.412	0.428	0.443	3.88%	3.50%
	Maximum displacement(mm)	23.67	23.12	22.86	2.32%	1.12%
	T1 (°)	3.72	3.61	3.59	2.96%	0.55%
	L1 (°)	1.91	1.89	1.86	1.05%	1.59%
S2	Vertebral cortical bone(MPa)	12.576	12.931	13.348	2.82%	3.22%
	Vertebral trabecular bone(MPa)	10.635	10.912	11.382	2.60%	4.31%
	Nucleus pulposus(MPa)	0.367	0.379	0.393	3.27%	3.69%
	Annulus fibrosus matrix(MPa)	0.425	0.438	0.451	3.06%	2.97%
	Maximum displacement(mm)	22.34	21.78	21.98	2.51%	0.92%
	T1 (°)	3.61	3.52	3.45	2.49%	1.99%
	L1 (°)	1.83	1.78	1.74	2.73%	2.25%

For the S1 model, when comparing the 1.0 mm mesh with the 0.8 mm mesh, the relative errors of peak stresses for each lumbar structure ranged from 2.67% to 3.88%, while the relative errors for maximum displacement and rotation angles of T1 and L1 ranged from 1.05% to 2.96%. When comparing the 1.2 mm mesh with the 1.0 mm mesh, the stress errors ranged from 2.52% to 3.50%, and the errors for maximum displacement and rotation angles of T1 and L1 ranged from 0.55% to 1.59%. For the S2 model, the stress errors between the 1.0 mm and 0.8 mm meshes ranged from 2.60% to 3.27%, with the errors for maximum displacement and rotation angles of T1 and L1 ranging from 2.49% to 2.73%; while between the 1.2 mm and 1.0

mm meshes, the stress errors ranged from 2.97% to 4.31%, and the errors for maximum displacement and rotation angles of T1 and L1 ranged from 0.92% to 2.25%. These data indicate that when the mesh size was refined to 1.0 mm, the relative errors for all stresses had strictly converged to within 5%. Therefore, considering both computational accuracy and efficiency, a standard mesh size of 1.0 mm was ultimately selected for subsequent finite element simulations, further ensuring the reliability of the model predictions.

2.9.2 Validation via Literature Comparison

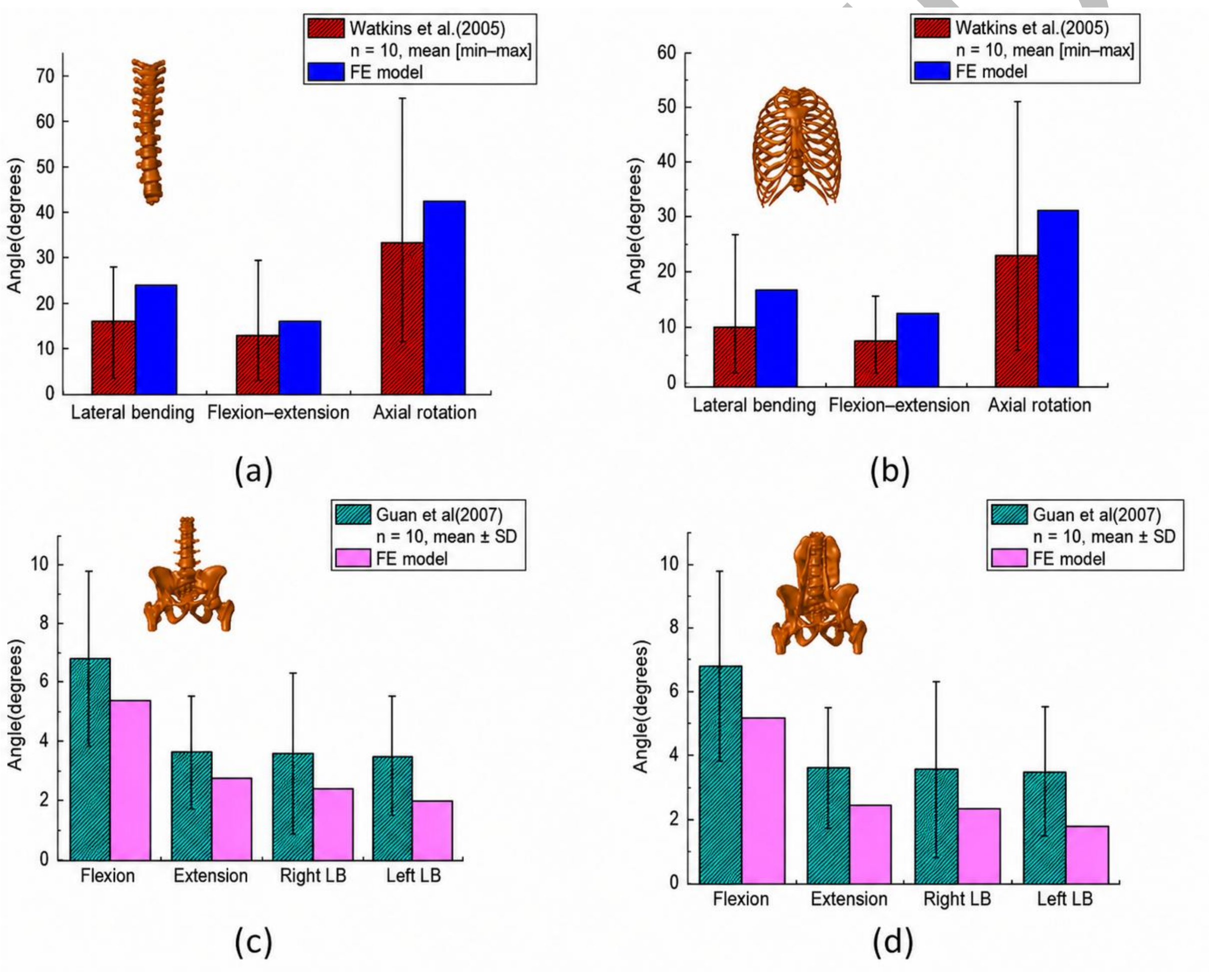

Figure 8: Comparison of finite element model range of motion (ROM) validation. (a) ROM of the thoracolumbar spine (T1-T12) without the thoracic cage under lateral bending, flexion-extension, and rotation conditions; (b) ROM of the thoracolumbar spine (T1-T12) with the thoracic cage under the corresponding conditions; (c) ROM of the lumbosacral spine (L1-S) without muscle attachment under lateral bending and flexion-extension conditions; (d) ROM of the lumbosacral spine (L1-S) with lumbar paravertebral muscles attached under lateral bending and

flexion-extension conditions.

Secondly, given the significant anatomical individual variability in pathological spinal kyphosis and the considerable difficulty in obtaining pathologically cadaveric specimens with perfectly matching geometry for in vitro mechanical testing, the data computed from this model were compared with experimental data from classic healthy in vitro spinal specimens.

To comprehensively evaluate the validity of the model, this study performed validation on the thoracolumbar spine (T1-T12) and lumbosacral spine (L1-S) segments under configurations with different anatomical accessory structures (with/without thoracic cage, with/without muscles). For the loading conditions of the thoracolumbar segment, referring to classic literature [33], a pure moment of 2 N·m was applied under lateral bending and flexion-extension conditions, while a pure moment of 5 N·m combined with a vertical preload of 50 N was applied under axial rotation conditions. For the lumbosacral segment, a pure moment of 4 N·m was applied to simulate lateral bending and flexion-extension movements[9].

The results, shown in Figure 9, indicate that although this model incorporates hyperkyphotic deformity characteristics, the displacement angles at key segments fell within the reasonable ranges reported in the literature. Furthermore, the introduction of the thoracic cage and lumbar paravertebral muscles in these validated segments effectively enhanced spinal stability. These findings also demonstrate that the established S1 and S2 models are suitable for subsequent finite element analysis of spinal kyphosis.Although the mesh-sensitivity, validation, and whole-spine simulations employ different loading magnitudes, they share identical meshes, material properties, contact definitions, and ligament formulations, differing only in the type and magnitude of applied load. The validation loads were selected to replicate classic in vitro protocols, confirming that the model reproduces physiologically realistic segmental responses under pure-moment loading; this validated mechanical behaviour was then carried over to the same modelling framework and applied to the loading conditions in the subsequent whole-spine kyphosis simulations, thereby ensuring mechanical comparability across all analysis stages.

2.9.3 Sensitivity Analysis of Material Parameters and Load Magnitude

Given that some material parameters were derived from the literature and may exhibit inter-individual variability, this study conducted a one-factor-at-a-time sensitivity analysis based on the baseline response of the intact S1 model under axial rotation loading. According to the baseline values listed in Table 1, the elastic moduli of muscle, costal cartilage, and cortical bone were perturbed individually, with each parameter varied in isolation by increasing or decreasing its baseline value by 20%. In addition, the axial rotation load magnitude for FE validation was independently adjusted to 120% and 80% of the baseline value. For each parameter perturbation, the maximum von Mises stresses of cortical bone, annulus fibrosus, and nucleus pulposus, as well as the maximum resultant displacement of the whole spine, were calculated and compared with the baseline results. The detailed results are presented in Table 3.

Table 3. One-factor sensitivity analysis of the main biomechanical indices of the S1 model under axial rotation

Perturbed parameter	**Parameter variation**	cortical bone stress (%)	annulus fibrosus stress (%)	Nucleus pulposus stress (%)	resultant spinal displacement (%)
Muscle elastic modulus	+20%	+1.7	+0.6	+0.5	+0.8
Muscle elastic modulus	−20%	−1.1	−0.4	−0.4	−0.6
Costal cartilage elastic modulus	+20%	+3.8	+1.6	+1.4	+2.0
Costal cartilage elastic modulus	−20%	−2.7	−1.3	−1.2	−1.7
Cortical bone elastic modulus	+20%	+8.6	+3.2	+3.1	+5.3
Cortical bone elastic modulus	−20%	−9.4	−3.5	−3.6	−5.5
Load magnitude	+20%	+7.7	+3.6	+4.0	+6.2
Load magnitude	−20%	−7.9	−3.4	−3.5	−6.6

The sensitivity analysis showed that when the material parameters and load magnitude were varied by ±20% from their baseline values, the maximum relative change in all evaluated biomechanical indices was 9.4%, and all changes remained below 10%. Among the investigated parameters, the cortical bone elastic modulus and load magnitude exerted relatively greater effects on the model outputs. Nevertheless, the overall variations remained limited, indicating that the predicted biomechanical responses were relatively insensitive to moderate perturbations in material properties and loading conditions. These findings support the robustness and numerical stability of the model and suggest that the selected material parameters and loading assumptions are reasonable for the present simulations.

2.10 Boundary Conditions, Loading Configuration, and Result Preprocessing

Regarding boundary condition settings, to simulate the physiological state of the human body in the standing position, all six degrees of freedom of the pelvis (ilium and sacrum) and portions of the femur were fully fixed.

Regarding the definition of the coordinate system, the global Cartesian coordinate system defaulted in Abaqus is not aligned with the anatomical planes of the human body. To enable direct comparison between the S1 and S2 models, a single anatomical local coordinate system was defined and uniformly adopted in this study. The origin of this local system was set at the center of the sacral endplate (pelvic reference point), with the X-axis pointing anteriorly, the Y-axis pointing to the subject's left, and the Z-axis oriented vertically upward. Accordingly, the X–Z plane forms the sagittal plane, the Y–Z plane forms the coronal plane, and the X–Y plane forms the transverse plane. In this system, rotation about the +Y axis corresponds to flexion; rotation about the +X axis corresponds to left lateral bending; and rotation about the +Z axis corresponds to left axial rotation.

Regarding load application, specific loading strategies were adopted for different physiological activity conditions. To simulate left and right axial rotation movements of the upper torso, couple loads of 20 N in opposite directions were applied to the bilateral transverse processes of the T1, T5, T8, T12, and L3 vertebrae[29],with a total resultant couple moment of 10.5 N·m. A directional concentrated load of 60 N was applied at a designated node of the T9 vertebra[37], and the direction of this load vector was varied to simulate typical daily activities of the upper torso, including forward flexion, extension, and left and right lateral bending.

In this study, the primary outcomes extracted are two metrics: the maximum displacement of the model and the relative rotation angle of the vertebrae with respect to the pelvis.The rotation angles reported in this study are defined as the rotation of each vertebra relative to the fixed pelvis, rather than the segmental range of motion between adjacent vertebrae. The rotation angles calculation still used the local coordinate system defined in Section 2.10 as the reference frame. In the preprocessing stage, local reference points for the pelvis and the target vertebrae were predefined. The pelvic reference point B served as the fixed reference, while the vertebral reference point A served as the moving reference. The nodal coordinates before and after loading were extracted and denoted as A, B, and A_1, B_1, respectively. The initial vector $V_0 = A - B$ and the post-loading vector $V_1 = A_1 - B_1$ were then constructed. The relative rotation angle between the two states was calculated as follows,where the magnitude of α represents the rotation angles in this study.

$$\alpha = \arccos\left(\frac{V0 \bullet V1}{|V0||V1|}\right) \times \frac{180}{\pi} \qquad (2)$$

3. Results

3.1 Global Spinal Displacement Comparison

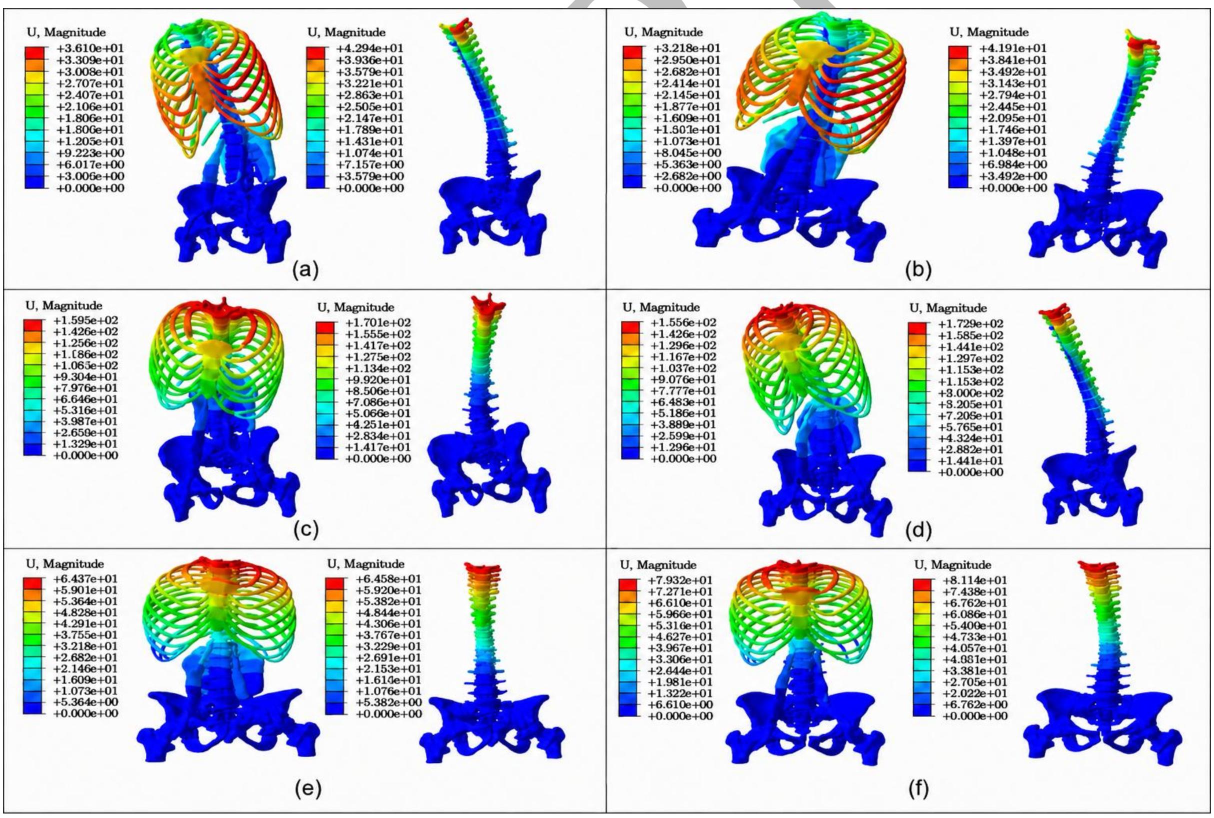

Figure 9. Displacement (mm) results of S1 and S2 under six loading conditions. (a) Left rotation; (b) Right rotation; (c) Left lateral bending; (d) Right lateral bending; (e) Flexion; (f) Extension.

To evaluate the biomechanical influence of the thoracic cage and passive muscles on the spine, the maximum spinal displacement of the S1 model was compared with that of the S2 model. The results are presented in Table 4.

Table 4. Maximum spinal displacements (mm) and relative changes between S1 and S2 models under various loading conditions

Loading Conditions	S1	S2	Relative Change Rate (%)
Left rotation	36.1	42.9	-15.9
Right rotation	32.2	41.9	-23.2
Left lateral bending	159.5	170.1	-6.2
Right lateral bending	155.6	172.9	-10.0
Flexion	64.4	64.6	-0.3
Extension	79.3	81.1	-2.2

***Note**: Relative change rate = (S1 - S2) / S2. Negative values indicate a decrease in the maximum displacement of S1 compared to S2.*

Under the six loading conditions, the maximum displacement of the S1 model was lower than that of the S2 model in all cases. Based on the loading plane, the above conditions were categorized into three types: rotation, lateral bending, and flexion-extension. The specific comparison results are as follows:

Under axial rotation conditions, the maximum spinal displacement of the S1 model showed the most significant change compared with the S2 model, with an average decrease of 19.6% (15.9% for left rotation, 23.2% for right rotation), representing the most pronounced reduction.

Under lateral bending conditions, the maximum spinal displacement decreased by an average of 8.1% (6.2% for left lateral bending, 10.0% for right lateral bending).

Under flexion-extension conditions, the maximum spinal displacement of the S1 model showed the least change compared with the S2 model, with an average decrease of only 1.3% (0.3% for flexion, 2.2% for extension).

3.2 Changes and Distribution of Vertebral Rotation Angles Relative to the Fixed Pelvis

Following the assessment of global stability, to further investigate the influence of the thoracic cage and passive lumbar paravertebral muscles on the regional behavior of the spine, the **rotation angles of each vertebra relative to the pelvis** of the S1 and S2 models was compared under flexion-extension, lateral bending, and axial rotation conditions. For quantitative analysis, the rotation angles in each motion plane was represented by the average of the bilateral symmetric movements (e.g., the average of flexion and extension). Additionally, to minimize potential manual errors during post-processing data extraction,the **rotation angles for each vertebra** was independently extracted three times, and the arithmetic mean of these three measurements was taken as the final result. Detailed comparative data are presented in Table 5.

Table 5: Vertebral rotation (°) relative to pelvis (S1/S2)

	Axial rotation			Lateral bending			Flexion-extension		
	S1	S2	Relative change rate (%)	S1	S2	Relative change rate (%)	S1	S2	Relative change rate (%)
T1	27.5	38.9	-29.31	21.8	24.4	-10.66	9.3	10	-7.00
T2	26.4	35.4	-25.42	23	24.7	-6.88	8.0	8.2	-2.44
T3	23.7	31.8	-25.47	22.3	24.1	-7.47	7.8	8.1	-3.70
T4	23.5	30.5	-22.95	23.2	24.6	-5.69	10.3	10.6	-2.83
T5	22.6	28.4	-20.42	20.8	22.2	-6.31	6.8	6.9	-1.45
T6	23.1	27.3	-15.38	20.4	21.6	-5.56	10.6	10.9	-2.75
T7	23.7	26.4	-10.23	23.3	24.9	-6.43	9.2	9.5	-3.16
T8	22.8	23.1	-1.30	23.7	25.3	-6.32	7.1	7.2	-1.39
T9	21.5	22.0	-2.27	23.0	24.4	-5.74	9.4	9.8	-4.08
T10	19.2	18.6	3.23	19.1	20.2	-5.45	8.6	8.8	-2.27
T11	16.3	15.7	3.82	17.3	18.4	-5.98	8.4	8.7	-3.45
T12	13.2	12.9	2.33	13.4	14.1	-4.96	9.1	9.3	-2.15
L1	10.7	10.4	2.88	10.2	10.6	-3.77	5.9	6.1	-3.28
L2	8.0	7.9	1.27	9.8	10.3	-4.85	7.2	7.4	-2.70
L3	5.0	4.8	4.17	7.4	7.8	-5.13	4.4	4.5	-2.22
L4	3.3	3.1	6.45	4.0	4.3	-6.98	2.3	2.4	-4.17
L5	1.3	1.2	8.33	1.8	2.1	-14.29	1.7	1.8	-5.56

Note: *Relative change rate = (S1 - S2) / S2. Negative values indicate S1 < S2, while positive values indicate S1 > S2.*

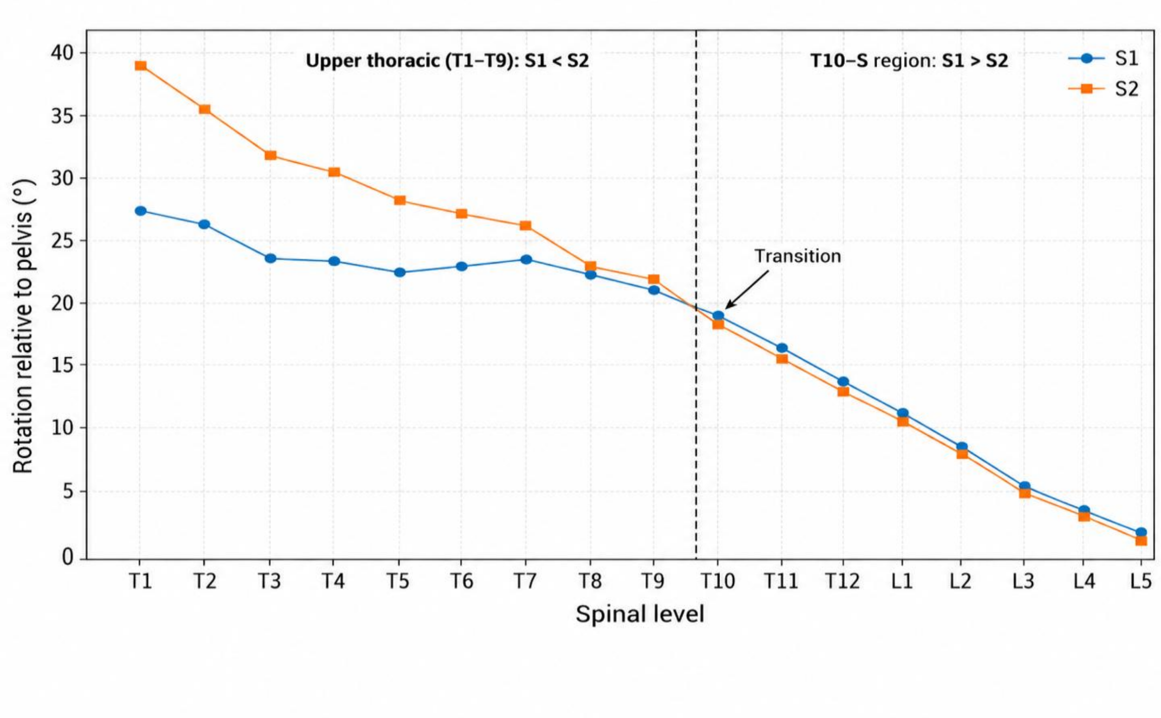

Figure.10 Rotation angles of each vertebra relative to the pelvis under axial rotation for the S1 and S2 models.

Under axial rotation, the rotation of each vertebra relative to the fixed pelvis was smaller in the S1 model than in the S2 model throughout the thoracic region (T1-T9, by 1.30% to 29.31%), the reduction exceeding 20% in the upper thoracic vertebrae (T1-T5). From the thoracolumbar junction downwards (T10-L5) this trend reversed and the rotation of the S1 model became larger than that of the S2 model (by 1.27% to 8.33%).

Under lateral bending conditions, the rotation of each vertebra relative to the fixed pelvis of the S1 model was lower than that of the S2 model across all segments (by 3.77% to 14.29%).

Under flexion-extension conditions, the rotation of each vertebra relative to the fixed pelvis of the S1 model was lower than that of the S2 model across all segments (by 1.39% to 7.00%).

4. Discussion

Although passive structures such as the thoracic cage and passive lumbar paraspinal muscles are important components in maintaining the balance of the human trunk system, few studies have deeply investigated their specific influence on the stability of the kyphotic spine. By comparing the S1 and S2 models, this study revealed that the stabilizing effects of the thoracic cage and passive lumbar paravertebral muscles on the kyphotic spine exhibit significant direction-specificity, presenting distinctly different biomechanical characteristics, particularly under rotation and flexion-extension conditions. Specifically, the maximum displacement reduction in the S1 model was most pronounced under rotation conditions (19.6%), whereas only a moderate reduction was observed under lateral bending conditions (8.1%). This prominent difference suggests that the intact thoracic cage and passive muscles can provide substantial kinematic constraint and potential load-sharing when resisting axial rotation. Mannen et al. [19]and Liebsch et al.[18]have clearly indicated in studies on healthy spines that the presence of an intact thoracic cage significantly increases the structural stiffness of the thoracolumbar spine in the axial rotational plane.Anatomically and mechanically, the thoracic cage forms a closed-loop three-dimensional structure comprising the sternum, ribs, costal cartilages, and costovertebral joints. During axial rotation, this structural arrangement provides pronounced geometric constraints and torsional load-sharing via bilateral ribs and costovertebral joints, thereby exerting the most substantial restriction on rotational displacement and upper thoracic rotation angles. The present study further demonstrates that this potent anti-rotational mechanism, contributed by passive structures such as the thoracic cage, remains effective even in the hyperkyphotic deformity state. This finding suggests that in clinical conservative treatment, utilizing orthotic braces to enhance the passive constraint of the thoracic cage holds important mechanical rationale for controlling abnormal spinal rotation.In stark contrast to its anti-rotational performance, the stabilizing contribution of passive structures under flexion-extension conditions was extremely weak (only a 1.3% reduction). This reveals a unique biomechanical characteristic of kyphotic deformity. Mechanically, flexion-extension is predominantly governed by sagittal bending moments. Sagittal stability in severe kyphosis relies more heavily on the neuromuscular control and active contraction of the back extensors and core musculature. In our model, the lumbar paraspinal muscles were simplified as passive linear-elastic materials, which inherently limited their ability to constrain flexion-extension.The present study hypothesizes that due to the patient's pre-existing severe sagittal anatomical deformity, the inherent stiffness of the spinal bony structure in the sagittal plane is likely already at a compensatory, very high level, rendering the additional auxiliary stiffness provided by passive structures negligible. This phenomenon indirectly demonstrates that relying solely on the tension of passive structures is far from sufficient to maintain sagittal balance in patients with severe kyphosis. To overcome the substantial flexion moment induced by the forward shift of the gravity line, powerful contraction of the active back muscles inevitably plays a dominant role. This aligns well not only with the clinical observation by Itoi et al. [11]that "back extensor strength increases significantly in women with severe kyphosis as a compensatory mechanism," but also further emphasizes that in clinical practice, compared to relying solely on passive bracing to maintain sagittal balance, strengthening the active back extensor muscles through rehabilitation training is the key strategy for counteracting deformity progression and preventing decompensation.

Based on the analysis of macroscopic global displacement patterns, this study further investigated regional segmental kinematic characteristics and identified a "paradoxical differentiation" phenomenon: after incorporating the thoracic cage and passive paravertebral muscles (S1 model), the overall spinal displacement and rotation angles of the middle and upper thoracic spine (T1–T7) decreased significantly (by 10.23%–29.31%) under rotational loading. In contrast, the rotation angles of the thoracolumbar to lumbosacral region (T10–L5) paradoxically increased (by 1.27%–8.33%), with the most pronounced increments occurring in the lower lumbar segments (L4–L5, by 6.45%–8.33%). This phenomenon may suggest a potential "anchoring–compensation" effect exerted by the thoracic cage–passive muscle complex: the rigid framework of the thoracic cage, in synergy with the tension network of the passive muscles, may help to enhance the stiffness of the middle and upper thoracic spine, thereby producing a "locking" effect on these segments to a certain extent. This is consistent with the findings of Morimoto et al. [Błąd! Nieznany argument przełącznika.], who noted that increased local stiffness significantly alters the load transmission patterns of the spine. Accordingly, it is inferred that once the middle and upper thoracic spine is "anchored," its capacity to dissipate strain energy may be reduced; consequently, the undissipated mechanical loads may be partially transmitted downward, potentially creating a tendency toward stress concentration at the thoracolumbar junction and lumbar segments, which in turn may drive a compensatory increase in rotation angles in these regions. From a clinical-pathological perspective, patients with severe kyphosis frequently present with strain at the thoracolumbar junction and accelerated degeneration of the lower lumbar spine (e.g., spondylolisthesis and degenerative disc disease). The "local anchoring–distal compensation" mechanical mechanism revealed in this study may offer a possible computational reference for explaining the high incidence of these clinical observations. Therefore, in the clinical evaluation and intervention of patients with severe kyphosis, clinicians may appropriately consider the phenomenon of downward stress migration induced by the rigidity of cranial structures; while addressing the primary deformity of the upper thoracic spine, protection of lower lumbar stability could also be regarded as a therapeutic goal worthy of attention in the treatment strategy.

This study has several limitations. First, the loading conditions were simplified, and gravitational effects and physiological axial preload were not explicitly incorporated, which may influence spinal rotation angles and load transfer among the vertebrae, intervertebral discs, and fixation structures. Second, the muscles were modeled as passive, linear-elastic, isotropic solids without active muscle recruitment. This assumption cannot fully reproduce the nonlinear, anisotropic, nearly incompressible, and length-dependent mechanical behavior of skeletal muscle and may affect the predicted force transmission and spinal stability. Future studies will incorporate gravity and physiological follower loads, together with nonlinear anisotropic muscle constitutive models and active muscle forces, to better reproduce the in vivo mechanical environment.

5. Conclusions

This study, based on S1 and S2 models, thoroughly investigated the influence of the thoracic cage and passive lumbar muscles on the stability of the kyphotic spine. The results show that the stabilizing effects of the thoracic cage and passive muscles exhibit direction-specificity and regional heterogeneity. Globally, passive structures substantially constrain the axial rotation of the spine but contribute limitedly to maintaining sagittal balance; overcoming the flexion moment remains highly dependent on the active contraction of muscles. Locally, passive structures **may induce** a "local anchoring and distal compensation" effect during rotation resistance: while effectively locking the middle and upper thoracic spine, they **may drive the redistribution** of non-dissipated stress concentrations downward, **which may increase** the compensatory mobility at the thoracolumbar junction and the lumbar segments below. Based on these biomechanical characteristics, this study provides theoretical evidence for the clinical management of kyphotic deformities: conservative treatment should adopt a dual-track strategy emphasizing both "passive bracing for rotation control" and "active strengthening of extensor muscles for anti-flexion," while maintaining long-term vigilance regarding the risk of secondary lower lumbar strain and degeneration **potentially associated with** downward stress migration.

Acknowledgement

The authors would like to express their gratitude to all reviewers who participated in the review.

Funding data

This work was supported by the National Natural Science Foundation of China (Grant No. 32260235).

Competing Interests

The authors have no relevant financial or non-financial interests to disclose.

Authors contribution

Jiameng Gong: Prepared the manuscript and executed the research.
Rongchang Fu: Obtained financing and designed the research program.
Jintao Li: Performed statistical analysis.
Kaitao Li: Interpreted the data.

Reference

[1]Anderson D.E., Mannen E.M., Tromp R. et al., The rib cage reduces intervertebral disc pressures in cadaveric thoracic spines by sharing loading under applied dynamic moments, J Biomech, 2018, 70:262-266.

[2]Andriacchi T., Schultz A., Belytschko T., Galante J., A model for studies of mecha nical interactions between the human spine and rib cage, J Biomech, 1974, 7:497-507.

[3]Arjmand N., Shirazi-Adl A., Model and in vivo studies on human trunk load partiti oning and stability in isometric forward flexions, J Biomech, 2006, 39:510-521.

[4]Baur D., Bieck R., Berger J. et al., Analysis of the paraspinal muscle morphology of the lumbar spine using a convolutional neural network, Eur Spine J, 2022, 31:774-782.

[5]Brasiliense L.B., Lazaro B.C., Reyes P.M., Dogan S., Theodore N., Crawford N.R., Biomechanical contribution of the rib cage to thoracic stability, Spine, 2011, 36:E1686-E1693, DOI: 10.1097/BRS.0b013e318219ce84.

[6]Bushberg J.T., Seibert J.A., Leidholdt E.M., Boone J.M., The Essential Physics of Medical Imaging, Lippincott Williams & Wilkins, 2011.

[7]Chabarova O., Selivonec J., Virtual modelling of the impact of torsional loading on osteoporotic vertebrae buckling, Acta Bioeng Biomech, 2024, 26(1):13-22, DOI: 10.371 90/abb-02392-2024-03.

[8]Frank A.P., Narayan Y., Thomas M. et al., Biomechanical properties of human lum bar spine ligaments, J Biomech, 1992, 25:1351-1356.

[9]Guan Y. et al., Moment-rotation responses of the human lumbosacral spinal column, J Biomech, 2007, 40:1975-1980.

[10]Isensee F., Jaeger P.F., Kohl S.A.A. et al., nnU-Net: a self-configuring method for deep learning-based biomedical image segmentation, Nat Methods, 2021, 18(2):203-211, DOI: 10.1038/s41592-020-01008-z.

[11]Itoi E., Sinaki M., Effect of back-strengthening exercise on posture in healthy women 49 to 65 years of age, Mayo Clin Proc, 1994, 69:1054-1059, DOI: 10.1016/s0025-6196(12)61372-x.

[12]Jia S., Lin L., Yang H. et al., The influence of the rib cage on the static and dynamic stability responses of the scoliotic spine, Sci Rep, 2020, 10:16916, DOI: 10.1038/s41598-020-73881-9.

[13]Jones A.C., Wilcox R.K., Finite element analysis of the spine: towards a framework of verification, validation and sensitivity analysis, Med Eng Phys, 2008, 30:1287-1304.

[14]Kang S., Chang M.C., Kim H., Kim J., Jang Y., Park D., Hwang J.M., The effects of paraspinal muscle volume on physiological load on the lumbar vertebral column: a finite-element study,Spine, 2021, 46:E1015-E1021, DOI: 10.1097/BRS.0000000000004014.

[15]Koelé M.C., Lems W.F., Willems H.C., The clinical relevance of hyperkyphosis: a narrative review, Front Endocrinol, 2020, 11:5, DOI: 10.3389/fendo.2020.00005.

[16]Li Z., Zhang B., Fang B., Gong H., Han Y., Pei S., Zhang S., Song G., Finite element analysis of a three-dimensional cervical spine model with muscles based on CT scan data, Comput Methods Biomech Biomed Engin, 2024, DOI: 10.1080/10255842.2024.2373928.

[17]Liebsch C., Graf N., Appelt K., Wilke H.J., The rib cage stabilizes the human thoracic spine: an in vitro study using stepwise reduction of rib cage structures, PLoS One, 2017, 12:e0178733, DOI: 10.1371/journal.pone.0178733.

[18]Liebsch C., Wilke H.J., How does the rib cage affect the biomechanical properties of the thoracic spine? A systematic literature review, Front Bioeng Biotechnol, 2022, 10:904539.

[19]Mannen E.M., Friis E.A., Sis H.L. et al., The rib cage stiffens the thoracic spine in a cadaveric model with body weight load under dynamic moments, J Mech Behav Biomed Mater, 2018, 84:258-264.

[20]Milletari F., Navab N., Ahmadi S.A., V-Net: Fully convolutional neural networks for volumetric medical image segmentation, In: 2016 Fourth International Conference on 3D Vision, IEEE, 2016, pp. 565-571.

[21]Morimoto M. et al., Biomechanical effects of thoracic flexibility and stiffness on lumbar spine loading: a finite element analysis study, World Neurosurg, 2024, 184:e282-e290.

[22]Nishida N., Ohgi J., Jiang F., Ito S., Imajo Y., Suzuki H., Funaba M., Nakashima D., Sakai T., Chen X., Finite element method analysis of compression fractures on whole-spine models including the rib cage, Comput Math Methods Med, 2019, 2019:8348631, DOI: 10.1155/2019/8348631.

[23]Oda I., Abumi K., Lu D., Shono Y., Kaneda K., Biomechanical role of the posterior elements, costovertebral joints, and rib cage in the stability of the thoracic spine, Spine, 1996, 21:2618-2624.

[24]Oda I., Abumi K., Cunningham B.W., Kaneda K., McAfee P.C., An in vitro human cadaveric study investigating the biomechanical properties of the thoracic spine, Spine, 2002, 27:E64-E70.

[25]Panjabi M.M., The stabilizing system of the spine. Part I. Function, dysfunction, adaptation, and enhancement, J Spinal Disord, 1992, 5:383-389, DOI: 10.1097/00002517-199212000-00001.

[26]Project PILLAR, Project PILLAR muscle segmentation guidelines, https://projectpillar.github.io/. Accessed 2 Apr 2026.

[27]Rahaman N., Baratin A., Arpit D. et al., On the spectral bias of neural networks, In: International Conference on Machine Learning, PMLR, 2019, pp. 5301-5310.

[28]Ronneberger O., Fischer P., Brox T., U-net: convolutional networks for biomedical image segmentation, In: Medical Image Computing and Computer-Assisted Intervention - MICCAI 2015, Springer International Publishing, 2015.

[29]Shen X., Finite element modeling and deformation analysis of the spine, Dissertati on, Kunming University of Science and Technology, 2012.

[30]Stokes I.A., Gardner-Morse M., Quantitative anatomy of the lumbar musculature, J Biomech, 1999, 32:311-316, DOI: 10.1016/s0021-9290(98)00164-x.

[31]US Army Research Laboratory, Verification and validation report for ATBM torso finite element model, Defense Technical Information Center, Washington D.C., 2018.

[32]Wang H., Fu R., Yang K., Kinetic characterization of adolescent scoliosis patients with Lenke 1B+, Acta Bioeng Biomech, 2025, 26(3):75-86, DOI: 10.37190/abb-02469-2024-03.

[33]Watkins R., Williams L., Ahlbrand S., Garcia R., Hedman T., Stability provided b y the sternum and rib cage in the thoracic spine, Spine, 2005, 30:1283-1286.

[34]Wesselink E.O., Elliott J.M., Coppieters M.W. et al., Convolutional neural networks for the automatic segmentation of lumbar paraspinal muscles in people with low back pain, Sci Rep, 2022, 12:13485.

[35]Yan W.T., Zhao G.P., Fang X.G. et al., Finite element modeling and analysis of th e L4-5 segment of the human lumbar spine, Chin J Biomed Eng, 2014, 31:612-61.

[36]Yang X.Z., Fu R.C., Li P.J. et al., Finite element analysis of the effect of trapeziu s on severe Lenke type 1 scoliotic spine, J Med Biomech, 2023, 38(6):1154-1159.

[37]Zhang B., Xiao J., Optimizer experimental design for deep learning model training, Electronic Production, 2024, 32:114-117.

[38]Zhu W., He X., Cheng K., Zhang L., Chen D., Wang X., Qiu G., Cao X., Weng X., Ankylosing spondylitis: etiology, pathogenesis, and treatments, Bone Res, 2019, 7:22, DOI: 10.1038/s41413-019-0057-8.